A resolvent analysis approach for the identification of dissipative scales in turbulent flows

By E. Ballouz

Reduced-order models attempt to mitigate the costs of direct numerical simulations (DNSs) by modeling the flow with its dominant coherent motions. To identify these length scales for the purpose of tuning restricted nonlinear turbulence models (Gayme & Minnick 2019) for the turbulent channel at $Re_\tau \approx 186$, we propose a modified resolvent analysis method formulated to compute the most amplified perturbations that feed off a transiently evolving streak. Traditional resolvent analysis uses the Navier-Stokes equations linearized about a mean velocity profile and Fourier-transformed in time to compute the maximally amplified velocity structures of a chosen frequency. Applied to channel flow, this method correctly identifies near-wall streaks as preferentially amplified structures, but it does not account for the transient growth of the streak, during which the growth of other length scales is triggered and the streak breaks down. We propose applying wavelet-based resolvent analysis, an extension developed to account for transient growth dynamics, to the Navier-Stokes equations linearized about a transiently growing streak—the primary coherent structure—to identify the most amplified secondary modes, that is, those most involved in the streak breakdown process. We compare these scales to those highlighted by dissipation spectra computed from DNS data and traditionally used to tune restricted nonlinear turbulence models.

1. Introduction

The coherent structures that dominate near-wall turbulence, streamwise rolls and streamwise streaks (Klebanoff *et al.* 1962; Bakewell Jr. & Lumley 1967; Kline *et al.* 1967; Blackwelder & Eckelmann 1979; Landahl 1980; Smith & Metzler 1983; Johansson *et al.* 1987) are believed to undergo a quasi-periodic cycle: streamwise streaks are amplified by streamwise vortices, meander, then collapse by shedding energy nonlinearly to smaller scales, which subsequently interact to regenerate streamwise vortices (Kim *et al.* 1971; Jiménez & Moin 1991; Robinson 1991; Hamilton *et al.* 1995; Waleffe 1997; Panton 2001; Adrian 2007; Smits *et al.* 2011; Jiménez 2018). In addition to accounting for the bulk of the turbulent kinetic energy near the wall, these structures influence the dynamics away from the wall and contribute significantly to shaping the entire mean turbulent velocity profile and the Reynolds stresses of the turbulent flow (Marusic 2001; Hutchins & Marusic 2007; Monty *et al.* 2007; Smits *et al.* 2011). Representing this cycle is crucial for the development of accurate low-order models of wall-bounded turbulent flows.

Restricted nonlinear turbulence (RNL) models attempt to reduce the degrees of freedom of a turbulent system so as to efficiently capture the dynamics of the most consequential scales of motion, that is, those that contribute most to shaping the turbulent mean profile and second-order statistics (Gayme & Minnick 2019; Minnick *et al.* 2023). RNL models solve a system of coupled equations: on the one hand, nonlinear equations that govern the streamwise-averaged mean velocity and pressure profile, denoted, respectively, by $\{\overline{U}_i^{x_1}\}_{i=1}^3$ and $\overline{P}^{x_1}$, and on the other hand, linear equations governing the

velocity and pressure fluctuations about this streamwise mean, denoted by u_1 (streamwise), u_2 (wall-normal), u_3 (spanwise) and p, respectively. But rather than include the contributions of all streamwise wave numbers to the nonlinear term of this equation, a subset of scales is represented and their evolution modeled by partial differential equations linearized about the time-evolving mean. These equations, nondimensionalized with the friction velocity u_τ and the channel half-height h, are given by

$$\frac{\partial \overline{U}_i^{x_1}}{\partial t} + \overline{U}_i^{x_1}\frac{\partial \overline{U}_i^{x_1}}{\partial x_j} + \frac{\partial \overline{P}^{x_1}}{\partial x_i} - \frac{1}{Re_\tau}\frac{\partial^2 \overline{U}_i^{x_1}}{\partial x_j \partial x_j} = -\frac{\partial \langle u_i u_j \rangle_{x_1}}{\partial x_j} \text{ and} \tag{1.1}$$

$$\frac{\partial u_i}{\partial t} + \frac{\partial p}{\partial x_i} - \frac{1}{Re_\tau}\frac{\partial^2 u_i}{\partial x_j \partial x_j} = -\overline{U}_i^{x_1}\frac{\partial u_i}{\partial x_j} - u_j\frac{\partial \overline{U}_i^{x_1}}{\partial x_j}, \tag{1.2}$$

where x_1, x_2 and x_3 denote the streamwise, wall-normal and spanwise directions, respectively, and $\langle\cdot\rangle_{x_i}$ denotes an average along the spatial direction x_i. The parameter $Re_\tau := u_\tau h/\nu$ is the friction Reynolds number, and ν is the kinematic viscosity. Only nonlinear interactions that contribute to the streamwise averaged mean are included—that is, the dyadic interactions between each scale and its streamwise conjugate. Only a subset of these scales are modeled, so

$$u_i = \sum_{k_1 \in \mathcal{T}} \hat{u}_i^{(k_1)}(x_2, x_3, t)e^{\mathrm{i}k_1 x_1} + \hat{u}_i^{(k_1)^*}(x_2, x_3, t)e^{-ik_1 x_1}, \tag{1.3}$$

where $\hat{u}_i^{(k_1)}$ is the streamwise Fourier transform of u_i corresponding to wave number k_1, $(\cdot)^*$ denotes the complex conjugate and $\mathcal{T}$ is a set of streamwise wave numbers. The pressure field is similarly represented. RNL models generate accurate mean velocity profiles for a range of Reynolds numbers; this confirms that a restricted number of large-scale structures play a dominant role in shaping the turbulent mean profile (Gayme & Minnick 2019). Likewise, quasi-linear dynamics seem to be sufficient at capturing the behavior of the large-scale fluctuations, insofar as they influence the mean velocity and shear profiles. The predictions can be further improved by including an additional nonlinear equation for an intermediate scale, $\tilde{k}_1$, forced by the nonlinear interaction between a dyadic pair within $\mathcal{T}$; this modification is dubbed augmented RNL (ARNL) (Minnick *et al.* 2023).

A pillar of the success of RNL models is the choice of scales to include in $\mathcal{T}$. To represent the self-sustaining process more fully, the model must capture the dominant coherent structures—streaks and rolls in channel flow—as well as the structures that modulate the growth of these streaks and dissipate their energy. The scales are chosen using dissipation or surrogate dissipation spectra computed from DNS vorticity data (Gorski *et al.* 1994; Jiménez 2012; Bretheim *et al.* 2015; Minnick & Gayme 2019). The latter differs from the former in that it does not consider cross-velocity gradients. Since computing reliable spectra is costly, especially for high Reynolds numbers, this work attempts to develop a framework that can identify these important scales without first relying on simulations first.

Since we seek scales of motion that play an eminent role in the generation and breakdown of the dominant coherent structures in channel flow, and since these scales seem to be well-represented with quasi-linear modes, resolvent analysis (McKeon & Sharma 2010; Moarref *et al.* 2013; McKeon 2017; Bae *et al.* 2021; Ballouz *et al.* 2024) emerges as a promising tool for tuning RNL models. Resolvent analysis casts the Navier-Stokes equations as a linear dynamical system for the velocity fluctuations about a mean flow

profile, in which the nonlinear term, rather than being ignored as in other linear analyses, appears as a forcing term actuating the system; the feedback between the velocity fluctuations and the forcing mode is ignored. The most perturbing input (forcing), the most amplified response (velocity and pressure fluctuations) and the kinetic energy amplification factor are then computed for this linearized system. To solve this optimization problem, a discretization of the resolvent map—the transfer function between the forcing and response modes—is constructed, and its singular value decomposition (SVD) computed. Due to its large memory cost, resolvent analysis is traditionally applied to systems exhibiting spatial and temporal homogeneity that have been Fourier transformed in time and the homogeneous spatial directions. This restricts the analysis to a particular scale of motion and wave speed. In the case of channel flow, where the directions of homogeneity are the streamwise and spanwise directions and time, the user of the method must select three Fourier parameters: spanwise and streamwise wavelength, and frequency. The chosen length scales tend to be the streamwise and spanwise streak spacings in the buffer layer (McKeon & Sharma 2010; Moarref *et al.* 2013; McKeon 2017; Bae *et al.* 2021); targeting these scales yields near-wall streamwise rolls as the most forcing structures and near-wall streamwise streaks as the most amplified response structures. Resolvent modes have been used more broadly to approximate the structure of large-scale motions and to identify dynamically important triadic interactions in turbulent channel flow at moderate Reynolds numbers (Huang *et al.* 2025).

Resolvent analysis can thus identify which scales undergo significant growth by interacting with the mean velocity and shear, and under external—relative to the chosen Fourier scales—forcing, which may come from nonlinear perturbations in realistic flows. The method has been used to explain the growth of streaks from rolls. In this work, we instead use the framework to identify the scales that play a direct role in the breakdown of streaks. We accomplish this by formulating the resolvent map for secondary velocity fluctuations about a modified base flow composed of a transiently evolving streak—the primary perturbation—added to a mean flow profile. Other works have studied the linear amplification properties of fluctuations about a nontraditional base flow, for example, a snapshot of a DNS or a streak obtained from optimal linear growth theory and frozen at its peak amplification (Lozano-Durán *et al.* 2021; Markeviciute & Kerswell 2024). One could also consider using a profile obtained from a DNS average conditioned on the presence of a streak. In this work, we make use of a modification of traditional resolvent analysis, wavelet-based resolvent analysis (Ballouz *et al.* 2024, 2025), which produces optimal modes that can additionally encode transient growth information. Indeed, this wavelet-based formulation allows one to identify secondary modes that exhibit a rapid initial growth, not just those that persist under the effect of sustained sinusoidal forcing, which traditional Fourier-based resolvent analysis exclusively considers. We argue that these modes that encode time information would more richly capture the cycle of streak generation and breakdown.

This work is organized as follows. In Section 2, we formulate the wavelet-based resolvent operator for both primary perturbations about the mean flow profile, and secondary perturbations about a composite base flow consisting of a mean velocity profile and a transiently growing primary perturbation. In Section 3, we compute and show resolvent dissipation spectra—estimates for the dissipation computed using the wavelet-based resolvent analysis framework—for different length scales, and compare them to surrogate dissipation spectra traditionally used in RNL and ARNL models. Finally, we discuss future work and give concluding remarks in Section 4.

2. Formulation

The focus of this work is to compute dissipation spectra for different scales of motion using an unconventional formulation of resolvent analysis, that is, one that computes the optimal transient energy growth of secondary perturbations about a primary perturbation (streak). To that end, we must first compute the mean flow profile $U_1(x_2)$ about which we define our primary and secondary perturbations. For one set of spectra, we use the laminar channel flow profile, which, for a wall-normal domain $x_2 \in [0, 2]$, is given by

$$U_1^{\text{laminar}}(x_2) = \frac{Re_\tau}{2} x_2(2 - x_2). \tag{2.1}$$

We also use the turbulent mean velocity and shear profiles with an equivalent friction velocity u_τ, which we compute with a DNS of the minimal flow unit and a larger channel. The details of these simulations are presented in Section 2.1. The formulation of resolvent analysis for our application is then presented in Section 2.2.

2.1. *Turbulent base flow*

To compute the mean flow profiles that are necessary for resolvent analysis, as well as the surrogate dissipation spectra to use as a benchmark for our resolvent-based method, we simulate the flow in two turbulent channels. The first is a minimal flow unit of size $L_1 \times L_2 \times L_3 = 1.72h \times 2h \times 0.86h$, where h is the channel half-height. The second is a larger channel of size $L_1 \times L_2 \times L_3 = 25.17h \times 2h \times 9.46h$. In both systems, the friction Reynolds number is $Re_\tau \approx 186$. Both flows are driven by a constant mean streamwise pressure gradient, and both flows are periodic in the streamwise and spanwise directions; we impose no-slip and no-penetration conditions at the walls.

For the minimal channel, we discretize the streamwise and spanwise directions uniformly using $N_1 = N_3 = 32$ grid points, amounting to streamwise and spanwise grid spacings of $\Delta x_1^+ \approx 10$ and $\Delta x_3^+ \approx 5$. In the wall-normal direction, the grid is of size $N_2 = 128$ and stretched according to a hyperbolic tangent distribution, amounting to a wall-normal spacing of $\min(\Delta x_2^+) \approx 0.17$ near the wall and $\max(\Delta x_2^+) \approx 7.6$ at the centerline. For the larger channel, we also use uniform grids of size $N_1 = 768$ and $N_3 = 290$ points in the streamwise and spanwise directions, respectively. This amounts to grid spacings of $\Delta x_1^+ = \Delta x_3^+ = 6.1$ in the streamwise and spanwise directions. The wall-normal grid is the same as in the minimal channel, that is, a hyperbolic tangent grid of size $N_2 = 128$. Throughout this text, the superscript + denotes quantities normalized with u_τ and ν.

In both cases, we solve the incompressible Navier-Stokes equations with a staggered, second-order accurate, central finite difference method in space (Orlandi 2000) and a fractional step method for pressure (Kim & Moin 1985). An explicit third-order-accurate Runge-Kutta method (Wray 1990) is used to advance the solution in time. This DNS code has been validated in Lozano-Durán & Bae (2016) and Bae *et al.* (2018, 2019). The laminar and turbulent mean profiles are shown in Figure 1.

2.2. *Resolvent formulation*

To compute the optimally amplified primary perturbation, or streak, we first formulate our wavelet-based resolvent operator using the incompressible Navier-Stokes equations for fluctuations about the mean flow and pressure fields $(U_1, 0, 0)$ and P, respectively. This procedure is described in detail in Ballouz *et al.* (2025) and summarized below. The laminar mean is obtained analytically [Eq. (2.1)], while the turbulent mean flow and pressure are computed by a streamwise, spanwise and time average of the DNS flow

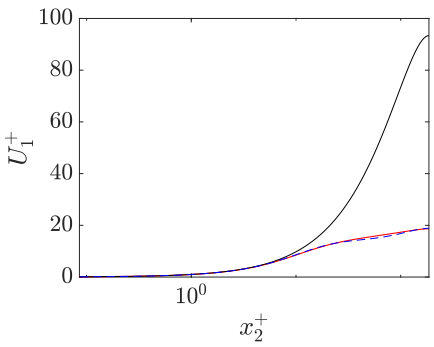

FIGURE 1. Laminar (black) and turbulent (blue, red) channel flow mean profiles. The blue dashed line corresponds to the minimal channel, and the red line corresponds to the larger channel.

data for the minimal and larger channel (Section 2.1). The equations for the velocity and pressure fluctuations, nondimensionalized with u_τ and h, Fourier-transformed in the streamwise and spanwise directions, discretized in the wall-normal direction and time, as well as wavelet-transformed in time. are

$$\frac{\partial u_i}{\partial t} + U_j \frac{\partial u_i}{\partial x_j} + u_j \frac{\partial U_i}{\partial x_j} = -\frac{\partial p}{\partial x_i} + \frac{1}{Re_\tau} \frac{\partial^2 u_i}{\partial x_j \partial x_j} + f_i, \quad \frac{\partial u_i}{\partial x_i} = 0. \tag{2.2}$$

Here f_i represents the nonlinear term in the x_i-momentum equation. The mean flow is either the laminar profile or the turbulent average obtained from the simulation described in Section 2.1. In both cases, $U_2 = U_3 = 0$, and U_1 is only a function of the wall-normal direction x_2. Equations (2.2) are Fourier-transformed in the x_1- and x_3-directions and discretised in x_2 and time. The time domain $[0, T]$ is periodic—*that is,* when constructing the resolvent operator for the discretised system, periodic boundary conditions are used for the temporal derivative matrix. For the minimal channel, $T = 22$, and for the larger one, $T = 5.5$. These are chosen to allow the computed resolvent-computed streak to decay to zero.

The discretized equations are further wavelet-transformed in time by premultiplying them by a discrete wavelet-transform operator $\boldsymbol{W}$. In this work, we use a single-level Daubechies-8 wavelet-transform (Daubechies 1992). The Daubechies wavelets and their corresponding scaling functions are compactly supported in time and form an orthonormal basis, resulting in a sparse banded and unitary operator $\boldsymbol{W}$ (Mallat 1999; Najmi 2012; Ballouz *et al.* 2024).

For a temporal grid of size N_t, a wall-normal grid of size N_2, and given streamwise and spanwise wave number pair $(k_1, k_3) = (2\pi k_1^\circ / L_1, 2\pi k_3^\circ / L_3)$, where $k_1^\circ,\ k_3^\circ \in Z$, we obtain the $N_t N_2$–dimensional system

$$\widetilde{\boldsymbol{D}_t}\widetilde{\boldsymbol{u}}_i + \widetilde{\boldsymbol{U}}_j \widetilde{\boldsymbol{D}_j}\widetilde{\boldsymbol{u}}_i + \widetilde{\boldsymbol{dU}_{ij}}\widetilde{\boldsymbol{u}}_j = -\widetilde{\boldsymbol{D}_i}\widetilde{\boldsymbol{p}} + \frac{1}{Re}\widetilde{\boldsymbol{D}^2_{jj}}\widetilde{\boldsymbol{u}}_i + \widetilde{\boldsymbol{f}}_i, \quad \widetilde{\boldsymbol{D}_i}\widetilde{\boldsymbol{u}}_i = 0. \tag{2.3}$$

Here, $\tilde{\boldsymbol{u}}_i$, $\tilde{\boldsymbol{p}}_i$ and $\tilde{\boldsymbol{f}}_i$ denote the discretized and transformed velocity and pressure fluctuations, and forcing, respectively. The forcing term represents the effect of the nonlinear term, which introduces energy to the chosen scales from other scales. These transformed quantities are functions of wall-normal position x_2, and the wavelet scale and shift parameters ℓ and m, which, respectively, represent the time interval and frequency

support of the wavelet mode (Ballouz *et al.* 2024). The modified time-derivative operator $\widetilde{\boldsymbol{D}_t} = \boldsymbol{W}\boldsymbol{D}_t\boldsymbol{W}^{-1}$ is constructed with the discrete wavelet-transform in time $\boldsymbol{W}$ and $\boldsymbol{D}_t$, a second-order-accurate central finite difference matrix in time. The matrix $\boldsymbol{D}_t$ is circulant to impose periodic boundary conditions at the edges of the temporal domain. The transformed spatial derivative operators are defined as follows: $\widetilde{\boldsymbol{D}_1} = \mathrm{i}k_1\boldsymbol{I}$, where $\boldsymbol{I}$ is the identity matrix of size $(N_2N_t) \times (N_2N_t)$; $\widetilde{\boldsymbol{D}_2} = \boldsymbol{D}_2$, which denotes a block diagonal second-order-accurate central finite difference operator on the staggered x_2– grid; and $\widetilde{\boldsymbol{D}_3} = \mathrm{i}k_3\boldsymbol{I}$ and $\widetilde{\boldsymbol{D}_{jj}^2} = -k_1^2\boldsymbol{I} + \boldsymbol{D}_2^2 - k_3^2\boldsymbol{I}$, where $\boldsymbol{D}_2^2$ denotes a second-order-accurate second-order-finite difference operator on the staggered x_2– grid. No-slip and no-penetration conditions are imposed at the bounds of the x_2–grid. The terms $\widetilde{\boldsymbol{U}}_j := \boldsymbol{W}\boldsymbol{U}_j\boldsymbol{W}^{-1}$ and $\widetilde{\boldsymbol{dU}}_{ij} := \boldsymbol{W}\boldsymbol{dU}_{ij}\boldsymbol{W}^{-1}$ are such that $\boldsymbol{U}_j$ and $\boldsymbol{dU}_{ij}$ are diagonal matrices with diagonal terms corresponding to U_j and dU_i/dx_j at each x_2 and time grid point, respectively. A more detailed description of these matrices is given in Ballouz *et al.* (2024) and Ballouz *et al.* (2025).

Equations 2.3 are then rearranged to reveal the resolvent operator $\widetilde{\boldsymbol{H}}^{(k_1,k_3)}$

$$\begin{bmatrix} \widetilde{\boldsymbol{u}}_1(x_2,\ell,m) \\ \widetilde{\boldsymbol{u}}_2(x_2,\ell,m) \\ \widetilde{\boldsymbol{u}}_3(x_2,\ell,m) \\ \widetilde{\boldsymbol{p}}(x_2,\ell,m) \end{bmatrix} = \widetilde{\boldsymbol{H}}^{(k_1,k_3)} \begin{bmatrix} \widetilde{\boldsymbol{f}}_1(x_2,\ell,m) \\ \widetilde{\boldsymbol{f}}_2(x_2,\ell,m) \\ \widetilde{\boldsymbol{f}}_3(x_2,\ell,m) \\ 0 \end{bmatrix}, \tag{2.4}$$

where the quantities in parentheses indicate the dimensions over which the flow quantities and forcing are discretized, and the superscripts denote the spatial Fourier parameters.

The traditional optimal forcing and response modes for channel flow are Fourier modes in time, that is, constant amplitude waves that peak at the wall-normal location where their streamwise wave speed matches the mean advection velocity $U_1(x_2)$ (McKeon & Sharma 2010; Moarref *et al.* 2013). In order to obtain a transiently evolving streak, we restrict the forcing to a wavelet pulse using a windowing post-matrix $\boldsymbol{B}$—which is a diagonal matrix that contains values of 1 for terms associated with the chosen shift and scale of the forcing pulse (Ballouz *et al.* 2025). We then compute the SVD of the windowed operator

$$\widetilde{\boldsymbol{H}}^{(k_1,k_3)}\boldsymbol{B} = \sum_j \sigma_j \tilde{\boldsymbol{\psi}}_j^{(k_1,k_3)} \tilde{\boldsymbol{\phi}}_j^{(k_1,k_3)^H}, \tag{2.5}$$

where $(\cdot)^H$ denotes the conjugate transpose. We index the singular values $\{\sigma_i\}_{i=1}^{4N_2N_t}$ such that $\sigma_1 \geq \sigma_2 \geq ... \geq 0$. Thus, the first right and left singular vectors $\tilde{\boldsymbol{\phi}}_{\boldsymbol{1}}^{(k_1,k_3)} = [\tilde{\boldsymbol{\phi}}_{\boldsymbol{1,1}}^{(k_1,k_3)^T}, \tilde{\boldsymbol{\phi}}_{\boldsymbol{1,2}}^{(k_1,k_3)^T}, \tilde{\boldsymbol{\phi}}_{\boldsymbol{1,3}}^{(k_1,k_3)^T}, \boldsymbol{0}^T]^T$ and $\tilde{\boldsymbol{\psi}}_{\boldsymbol{1}}^{(k_1,k_3)} = [\tilde{\boldsymbol{\psi}}_{\boldsymbol{1,1}}^{(k_1,k_3)^T}, \tilde{\boldsymbol{\psi}}_{\boldsymbol{1,2}}^{(k_1,k_3)^T}, \tilde{\boldsymbol{\psi}}_{\boldsymbol{1,3}}^{(k_1,k_3)^T}, \tilde{\boldsymbol{\psi}}_{\boldsymbol{1,p}}^{(k_1,k_3)^T}]^T$ are, respectively, the optimal pulse-like forcing mode and its associated transient response. The SVD is computed such that

$$\int_\ell \int_m \int_0^2 |\tilde{\boldsymbol{\psi}}_{\boldsymbol{1,1}}|^2 + |\tilde{\boldsymbol{\psi}}_{\boldsymbol{1,2}}|^2 + |\tilde{\boldsymbol{\psi}}_{\boldsymbol{1,3}}|^2 dx_2 dm d\ell = 1, \tag{2.6}$$

$$\int_\ell \int_m \int_0^2 |\tilde{\boldsymbol{\phi}}_{\boldsymbol{1,1}}|^2 + |\tilde{\boldsymbol{\phi}}_{\boldsymbol{1,2}}|^2 + |\tilde{\boldsymbol{\phi}}_{\boldsymbol{1,3}}|^2 dx_2 dm d\ell = 1. \tag{2.7}$$

To find the most amplified secondary scales—those that grow at the expense of a transiently growing primary perturbation—we formulate the resolvent operator for perturbation about a new base flow, $\breve{\boldsymbol{U}} = \boldsymbol{U} + \kappa\tilde{\sigma}_1\boldsymbol{\psi}_1$, where $\boldsymbol{\psi}_1$ is the inverse-Fourier- and

inverse-wavelet-transformed optimal response mode obtained from the previous step—summed with the inverse-transform of its conjugate to ensure the perturbation is real—and κ denotes a real positive scaling parameter. When using the turbulent profile, κ is chosen so that $\kappa^2 \approx 3.54$, the x_2–integrated magnitude of the ensemble-averaged streamwise Reynolds stress $\overline{u_1 u_1}$ obtained from DNS. When using the laminar profile as a proxy, because we are attempting to avoid DNS-dependent quantities, we set $\kappa = 1$, which amounts to a perturbation of magnitude u_τ. The discretized, Fourier- and wavelet-transformed equations for this new system are

$$\begin{aligned}
&\widetilde{\boldsymbol{D}_t}\widetilde{\boldsymbol{u}}_i \\
&\quad + \left(\breve{\widetilde{\boldsymbol{U}}}_j^{(s_1,s_3)}\,\widetilde{\boldsymbol{D}}_j^{(k_1-s_1,k_3-s_3)}\widetilde{\boldsymbol{u}}_i^{(k_1-s_1,k_3-s_3)} + \widetilde{\boldsymbol{u}}_j^{(k_1-s_1,k_3-s_3)}\widetilde{\boldsymbol{d}\breve{\boldsymbol{U}}}_{ij}^{(s_1,s_3)}\right) \\
&\quad + \left(\breve{\widetilde{\boldsymbol{U}}}_j^{(-s_1,s_3)}\,\widetilde{\boldsymbol{D}}_j^{(k_1+s_1,k_3-s_3)}\widetilde{\boldsymbol{u}}_i^{(k_1-s_1,k_3-s_3)} + \widetilde{\boldsymbol{u}}_j^{(k_1+s_1,k_3-s_3)}\widetilde{\boldsymbol{d}\breve{\boldsymbol{U}}}_{ij}^{(-s_1,s_3)}\right) \\
&\quad + \left(\breve{\widetilde{\boldsymbol{U}}}_j^{(s_1,-s_3)}\,\widetilde{\boldsymbol{D}}_j^{(k_1-s_1,k_3+s_3)}\widetilde{\boldsymbol{u}}_i^{(k_1-s_1,k_3+s_3)} + \widetilde{\boldsymbol{u}}_j^{(k_1-s_1,k_3+s_3)}\widetilde{\boldsymbol{d}\breve{\boldsymbol{U}}}_{ij}^{(s_1,-s_3)}\right) \\
&\quad + \left(\breve{\widetilde{\boldsymbol{U}}}_j^{(-s_1,-s_3)}\,\widetilde{\boldsymbol{D}}_j^{(k_1+s_1,k_3+s_3)}\widetilde{\boldsymbol{u}}_i^{(k_1-s_1,k_3-s_3)} + \widetilde{\boldsymbol{u}}_j^{(k_1+s_1,k_3+s_3)}\widetilde{\boldsymbol{d}\breve{\boldsymbol{U}}}_{ij}^{(-s_1,-s_3)}\right) \\
&\qquad = -\widetilde{\boldsymbol{D}_i}\widetilde{\boldsymbol{p}} + \frac{1}{Re}\widetilde{\boldsymbol{D}_{jj}^2}\widetilde{\boldsymbol{u}}_i + \breve{\boldsymbol{f}}_i, \quad (2.8)
\end{aligned}$$

$$\widetilde{\boldsymbol{D}_i}\widetilde{\boldsymbol{u}}_i = 0.$$

Here, the streamwise and spanwise wave numbers used to transform the equations are (k_1, k_3)—the target scale. Wave numbers (s_1, s_3) characterize the primary perturbation $\kappa\boldsymbol{\psi}$. Quantities denoted by $\widetilde{(\cdot)}$ (without superscript) are associated with wave numbers (k_1, k_3); quantities denoted by $\widetilde{(\cdot)}^{(q_1,q_3)}$ are associated with wave numbers (q_1, q_3). The derivatives $\tilde{\boldsymbol{D}}_{\boldsymbol{1}}^{(q_1,q_3)}$ and $\tilde{\boldsymbol{D}}_3^{(q_1,q_3)}$ (with superscripts) correspond to $\mathrm{i}q_1\boldsymbol{I}$ and $\mathrm{i}q_3\boldsymbol{I}$, respectively, and $\tilde{\boldsymbol{D}}_2^{(q_1,q_3)} = \tilde{\boldsymbol{D}}_2$. The terms $\breve{\widetilde{\boldsymbol{U}}}_j^{(s_1,s_3)} := \boldsymbol{W}\widehat{\breve{\boldsymbol{U}}_{\boldsymbol{j}}}^{(s_1,s_3)}\boldsymbol{W}^{-1}$ and $\widetilde{\boldsymbol{d}\breve{\boldsymbol{U}}}_{ij} := \boldsymbol{W}\widehat{\boldsymbol{d}\breve{\boldsymbol{U}}}_{ij}^{(s_1,s_3)}\boldsymbol{W}^{-1}$ are such that $\hat{\breve{\boldsymbol{U}}}_j^{(s_1,s_3)}$ and $\boldsymbol{d}\hat{\breve{\boldsymbol{U}}}_{ij}^{(s_1,s_3)}$ are diagonal matrices with diagonal terms, respectively, corresponding to $\widehat{\breve{U}_j}$ and $\widehat{d\breve{U}_i/dx_j}$, the Fourier transforms of the mean velocity and shear associated with wave numbers (s_1, s_3), at each point on the x_2 and time grids.

The target scale (k_1, k_3) is coupled to scales $(k_1 - s_1, k_3 - s_3)$ and $(k_1 + s_1, k_3 + s_3)$ via the composite base flow. The dynamics of these supplementary scales must also be considered to close the system. Let $\mathcal{S}$ denote the set of the coupled wave number pairs considered, and $N_s = |\mathcal{S}|$. The target wave number pair must always be an element of $\mathcal{S}$. The resolvent operator in this system is thus an $4N_tN_2N_s \times 4N_tN_2N_s$–dimensional complex matrix. For values $N_s = 1$ and $\mathcal{S} = \{(k_1, k_3)\}$, we re-obtain the modes given by Eq. (2.5), with $\boldsymbol{B} = \boldsymbol{I}$. For $\mathcal{S} = \{(k_1 - s_1, k_3 - s_3), (k_1, k_3), (k_1 + s_1, k_3 + s_3)\}$, for example, $N_s = 3$, the modes are arranged into three $4N_tN_2$–long subvectors, each corresponding

to a scale in $\mathcal{S}$, and the resolvent operator has the form

$$\breve{\boldsymbol{H}}^{(k_1,k_3)} = \begin{bmatrix} \tilde{\boldsymbol{H}}^{(k_1-s_1,k_3-s_3)} & \boldsymbol{G}^{(k_1,k_3,-s_1,-s_3)} & \boldsymbol{0}_{4N_2N_t\times 4N_2N_t} \\ \boldsymbol{G}^{(k_1-s_1,k_1-s_3,,s_1,s_3)} & \tilde{\boldsymbol{H}}^{(k_1,k_3)} & \boldsymbol{G}^{(k_1+s_1,k_1+s_3,-s_1,-s_3)} \\ \boldsymbol{0}_{4N_2N_t\times 4N_2N_t} & \boldsymbol{G}^{(k_1,k_3,s_1,s_3)} & \tilde{\boldsymbol{H}}^{(k_1+s_1,k_3+s_3)} \end{bmatrix}, \quad (2.9)$$

where $\boldsymbol{G}^{(q_1,q_3,r_1,r_2)}$ is a $4N_tN_2 \times 4N_tN_2$-dimensional complex matrix defined as

$$\boldsymbol{G}^{(q_1,q_3,r_1,r_2)} = \begin{bmatrix} \widetilde{\breve{\boldsymbol{U}}}_j^{(r_1,r_3)} \widetilde{\boldsymbol{D}}_j^{(q_1,q_3)} + \widetilde{\boldsymbol{d}\breve{\boldsymbol{U}}}_{11}^{(r_1,r_3)} & \widetilde{\boldsymbol{d}\breve{\boldsymbol{U}}}_{12}^{(r_1,r_3)} & \widetilde{\boldsymbol{d}\breve{\boldsymbol{U}}}_{13}^{(r_1,r_3)} & \boldsymbol{0} \\ \widetilde{\boldsymbol{d}\breve{\boldsymbol{U}}}_{21}^{(r_1,r_3)} & \widetilde{\breve{\boldsymbol{U}}}_j^{(r_1,r_3)} \widetilde{\boldsymbol{D}}_j^{(q_1,q_3)} + \widetilde{\boldsymbol{d}\breve{\boldsymbol{U}}}_{22}^{(r_1,r_3)} & \widetilde{\boldsymbol{d}\breve{\boldsymbol{U}}}_{23}^{(r_1,r_3)} & \boldsymbol{0} \\ \widetilde{\boldsymbol{d}\breve{\boldsymbol{U}}}_{31}^{(r_1,r_3)} & \widetilde{\boldsymbol{d}\breve{\boldsymbol{U}}}_{32}^{(r_1,r_3)} & \widetilde{\breve{\boldsymbol{U}}}_j^{(r_1,r_3)} \widetilde{\boldsymbol{D}}_j^{(q_1,q_3)} + \widetilde{\boldsymbol{d}\breve{\boldsymbol{U}}}_{33}^{(r_1,r_3)} & \boldsymbol{0} \\ \boldsymbol{0} & \boldsymbol{0} & \boldsymbol{0} & \boldsymbol{0} \end{bmatrix}. \quad (2.10)$$

A similar form is obtained in Padovan *et al.* (2020), which considers the coupling between different temporal frequencies. The "central"—target—mode is specified with the superscript $(\cdot)^{(k_1,k_3)}$, and the coupling with the additional modes in $\mathcal{S}$ is also captured by this resolvent operator.

We compute the SVD of this operator using the laminar and turbulent mean profiles and their respective optimal transient streak computed using the decomposition given in Eq. (2.5), for both the minimal and the larger channel, at $Re_\tau = 186$. The results are presented in the following section. Let $\breve{\sigma}_1^{(k_1,k_3)}$ denote the largest singular value of $\breve{\boldsymbol{H}}^{(k_1,k_3)}$, and $\breve{\boldsymbol{\psi}}_1^{(k_1,k_3)} = [\breve{\boldsymbol{\psi}}_{1,1}^{(k_1,k_3)^T}, \breve{\boldsymbol{\psi}}_{1,2}^{(k_1,k_3)^T}, \breve{\boldsymbol{\psi}}_{1,3}^{(k_1,k_3)^T}, \breve{\boldsymbol{\psi}}_{1,p}^{(k_1,k_3)^T}]^T$ the subvectors of the principal response mode corresponding to the central, or target, Fourier mode. The subvectors corresponding to the additional scales are not used in this work.

We note that the scales at the bounds of the $\mathcal{S}$ set are only coupled to one other mode via the primary perturbation or its conjugate, rather than two. To ensure the convergence of the computed modes, we must increase N_s and verify that these incompletely coupled modes undergo negligible linear amplification and that their incomplete modeling affects the remaining captured scales little. Denoting such a one-way-coupled scale by (r_1, r_3), we aim for $\breve{\boldsymbol{\psi}}_{\boldsymbol{1}}^{(r_1,r_3)} \approx \boldsymbol{0}$.

3. Secondary amplification spectra

In this section, we compare resolvent dissipation spectra to DNS surrogate dissipation spectra for different wave numbers at different wall-normal heights. In particular, we compute

$$\alpha^2(k_1,x_2) = k_1 \sum_{k_3} \breve{\sigma}^{(k_1,k_3)^2} \int_0^\tau \left|\partial_{x_2}\breve{\psi}_{1,3}^{(k_1,k_3)} - \mathrm{i}k_3\breve{\psi}_{1,2}^{(k_1,k_3)}\right|^2 + \left|\mathrm{i}k_3\breve{\psi}_{1,1}^{(k_1,k_3)} - \mathrm{i}k_1\breve{\psi}_{1,3}^{(k_1,k_3)}\right|^2 + \left|\mathrm{i}k_1\breve{\psi}_{1,2}^{(k_1,k_3)} - \partial_{x_2}\breve{\psi}_{1,1}^{(k_1,k_3)}\right|^2 dt \quad (3.1)$$

after computing the SVD of $\breve{\boldsymbol{H}}^{(k_1,k_3)}$ for different central wave numbers (k_1, k_3), using both the laminar and turbulent mean profiles and the corresponding optimal transient

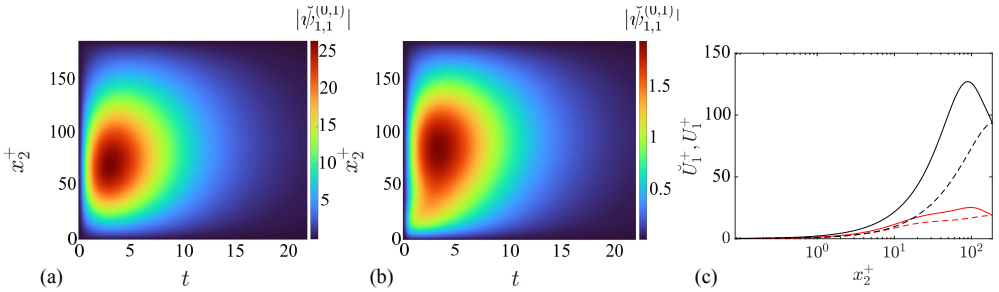

FIGURE 2. Magnitude of the streamwise component of the primary perturbation (equivalently, optimal linear streak) $\tilde{\sigma}_1^{(0,1)}|\tilde{\boldsymbol{\psi}}_{1,1}^{(0,1)}|$ computed for the minimal channel using (a) the laminar mean profile and (b) the turbulent mean profile at $Re_\tau = 186$. (c) The streamwise base flow $\breve{U}_1$ at peak t and x_3 for the laminar (solid black) and turbulent (solid red) cases, with the original laminar (dashed black) and turbulent (dashed red) shown for comparison.

streak for both the minimal and larger channels. The quantity $\tau \leq T$ is a maximum integration time and allows us to limit the analysis to the initial growth of the modes.

We compare the α^2–spectrum to the surrogate dissipation spectrum obtained from DNS. The nondimensionalized surrogate dissipation is defined as in Jiménez (2012), that is,

$$E_\omega(k_1, x_2) = \frac{1}{Re_\tau} k_1 \left(\frac{1}{L_3} \int_0^{L_3} \overline{\hat{\omega}_1^{(k_1)} \hat{\omega}_1^{(k_1)}} + \overline{\hat{\omega}_2^{(k_1)} \hat{\omega}_2^{(k_1)}} + \overline{\hat{\omega}_3^{(k_1)} \hat{\omega}_3^{(k_1)}} dx_3 \right), \tag{3.2}$$

where $\hat{\omega}_i^{(k_1)}$ denotes the x_i–component of the vorticity, Fourier-transformed in the streamwise direction and corresponding to streamwise wave number k_1. This quantity is used in Gayme & Minnick (2019) and Minnick *et al.* (2023) to tune RNL and ARNL models.

3.1. *Minimal channel*

For the minimal channel, we choose $N_t = 256$, $T = 44$ and $N_2 = 80$. We use a single-stage Fejér-Korovkin wavelet-transform of filter size 22. To compute the primary, we choose $(k_1^\circ, k_3^\circ) = (0, 1)$ and restrict the forcing mode to the scaling function with shift parameter $m = 0$, that is, centered a $t \approx 0$. The optimal response mode and transient primary perturbation (streak) is shown in Figure 2, along with the modified base flow. For the secondary perturbations, we consider two cases: $N_s = 1$ and $N_s = 13$. In the former case, to produce transiently growing modes, we window the forcing to the scaling function $m = 0$ as when we compute the primary perturbation. In the latter case, the forcing is unwindowed and the transient growth of the secondary target scales is governed by that of the primary streak. Choosing $N_s = 13$ implies that we additionally model the linear dynamics of a set $\mathcal{S} = \{(k_1^\circ, k_3^\circ + j)\}_{j=-6}^{6}$. We found that changing this set—that is, increasing N_s or decreasing N_s slightly—did not change the results significantly. The target modes for which α^2 is computed are $k_1^\circ, k_3^\circ \in \{0,\ 1,\ \ldots,\ 7\}$. An example mode is shown in Figure 3 to illustrate the effect of the primary streak interaction on the mode shape. To compute α, we use $\tau = 3.4$, which corresponds to the kinetic energy peak of the primary perturbation $\boldsymbol{\psi}_1^{(0,1)}$ for both the laminar and turbulent means.

The results for $N_s = 1$ are shown in Figure 4. In general, the α–spectra obtained from the laminar and turbulent means are very similar. Both exhibit peak dissipation for $k_1^\circ = 6$ at the wall [Figure 4(a, b)]. Lower wave numbers also exhibit significant α^2,

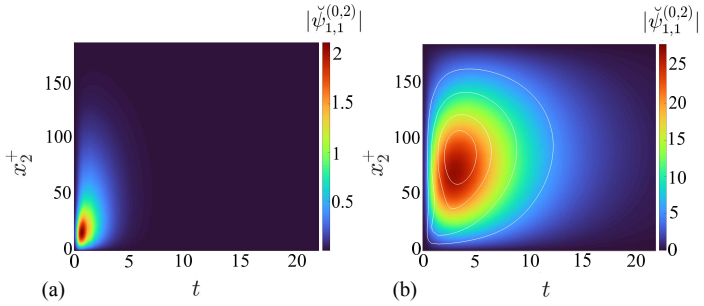

FIGURE 3. Magnitude of the streamwise component of a secondary perturbation $|\sigma^{(0,2)}\breve{\boldsymbol{\psi}}^{(0,2)}_{1,1}|$ computed using the turbulent mean profile of the larger channel at $Re_\tau = 186$, for (a) $N_s = 1$ (b) $N_s = 13$. White lines in (b) indicate the primary streak contours (25%, 50%, 75% and 90% of the maximum).

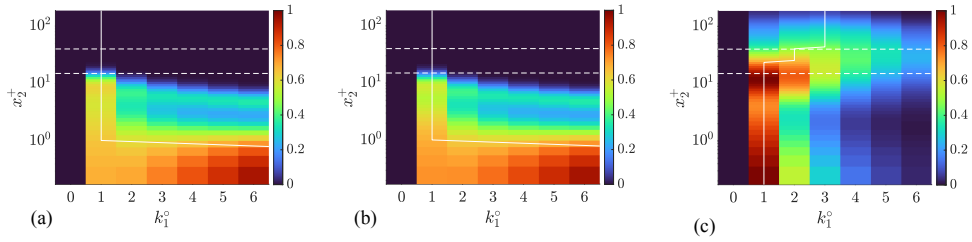

FIGURE 4. Minimal channel dissipation α^2 with $N_s = 1$, normalized by the maximum over x_2 and k_1 and using (a) the laminar mean and (b) the turbulent mean; (c) represents the surrogate dissipation from the DNS of the minimal channel. The values are normalized by the maximum value across all k_1° and x_2; the solid white line represents the x_2–local maximum across k_1° values, and the dashed horizontal lines mark the limits of the buffer layer $x_2^+ = 15$ and $x_2^+ = 40$.

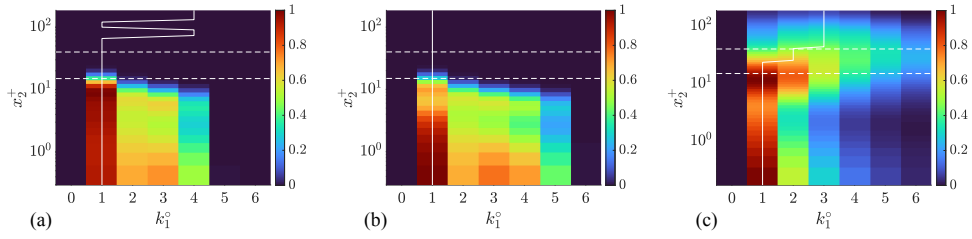

FIGURE 5. Minimal channel dissipation α^2 with $N_s = 13$, normalized by the maximum over x_2 and k_1 and using (a) the laminar mean and (b) the turbulent mean; (c) represents the surrogate dissipation from the DNS of the minimal channel. The values are normalized by the maximum value across all k_1° and x_2; the solid white line represents the x_2–local maximum across k_1° values, and the dashed horizontal lines mark the limits of the buffer layer $x_2^+ = 15$ and $x_2^+ = 40$.

especially for $x_2^+ < 1$, and we note that α^2 decreases as k_1° decreases. In contrast, the pre-multiplied surrogate dissipation spectrum computed using DNS data exhibits a peak at $k_1^\circ = 1$ at a higher $x_2^+ \approx 11$. The surrogate dissipation follows the opposite trend in k_1°, that is, E_ω decreases monotonically as k_1 increases. To match the methodology in

Jiménez (2012) and Gayme & Minnick (2019), we also show the most prominent scale in the α– and E_ω–spectra at each x_2–location. The α–spectra fail to capture the prominence of larger scales close to the wall ($x_2^+ < 1$), though $k_1^\circ = 1$ dominates for $x_2^+ \geq 1$. In the DNS-based results, $k_1^\circ = 1$ dominates in the near-wall region through the middle of the buffer layer, while scales $k_1^\circ = 2,\ 3$ take over the surrogate dissipation at the top of the buffer layer and in the outer region.

In Figure 5, we show the α–spectra computed with $N_s = 13$, that is, after considering the interaction with both the mean profile and the primary perturbation, the transiently evolving minimal channel streak, which is constant in the streamwise direction and once-periodic in the spanwise direction. The results are in closer agreement with the DNS-based surrogate dissipation spectrum: For both the laminar and turbulent means, the $k_1^\circ = 1$ scale dominates until the top of the buffer layer. The dissipation α^2 peaks at $x_2^+ \approx 10$ for the laminar case and at the wall for the turbulent case, though for the former, the dissipation is still significant throughout the near-wall region. Using the turbulent mean highlights a larger range of k_1°, up to $k_1^\circ = 5$, in closer agreement with the E_ω spectrum.

For the minimal channel, considering the coupling with the primary streak greatly improves the resolvent dissipation spectrum. This version of the α–spectra shares key characteristics with the surrogate dissipation spectrum: the preeminent role of $k_1^\circ = 1$, and to a lesser degree, the cluster of wave numbers $k_1^\circ \in \{2,\ 3,\ 4\}$. Interestingly, the choice of a laminar mean or turbulent mean profile and their corresponding primary perturbation does not change the resolvent dissipation spectrum. Though the primary perturbations in both cases are similar, they do not dominate the base flow [Figure 2], and we expect the differences between the spectra to be starker. For the purpose of picking scales for RNL, the spectra for $N_s = 13$ point to a similar choice of streamwise wave numbers as the DNS-based surrogate dissipation spectrum.

However, the reduced complexity of RNL would be more useful for larger domains and higher Reynolds numbers, where the self-sustaining cycle is less clearly observed than in the minimal channel. In turbulent systems, the linear growth of resolvent modes is quickly curtailed by nonlinear energy transfer to other scales (Ballouz *et al.* 2025); in a larger channel, where more scales participate in the energy cascade, linear dynamics may play an even lesser role, and optimal linear growth methods may not model the self-sustaining cycle accurately enough to produce useful spectra (Jiménez 2018). The timescale of the initial algebraic growth has been argued to scale as $O(1/Re_\tau)$ (Schmid *et al.* 2002), and thus structures growing under linear dynamics may trigger turbulent behavior earlier and persist for shorter times as Reynolds number increases. To check the useability of resolvent-based spectra, we repeat the experiment above for the larger channel.

3.2. *Larger channel*

For the larger channel, we choose $N_t = 256$, $T = 11$ and $N_2 = 80$. We use a three-stage Fejér-Korovkin wavelet-transform with filter size 22. To compute the primary, we choose $(k_1^\circ, k_3^\circ) = (5, 18)$, which corresponds to $(\lambda_1^+, \lambda_3^+) \approx (1000, 100)$. We restrict the forcing mode to the wavelet function with scale parameter $\ell = 3$ and shift parameter $m = 0$. Since the Fejér-Korovkin wavelets are approximate band-pass filters, this windowing process targets frequencies $\omega \in 2\pi N_t/T[1/2^{\ell+1}, 1/2^\ell]h/u_\tau = [9.1, 18.3]h/u_\tau$ (Ballouz *et al.* 2024), which corresponds to wave speeds of $\omega/k_1 \in [7.8, 15.6]/u_\tau$. The resolvent modes computed using these length scales tend to peak where their wave speed matches the average streamwise velocity (McKeon & Sharma 2010; Moarref *et al.* 2013); wave speeds targeted by the windowed forcing thus correspond to a region $x_2^+ \in [9, 50]$, which

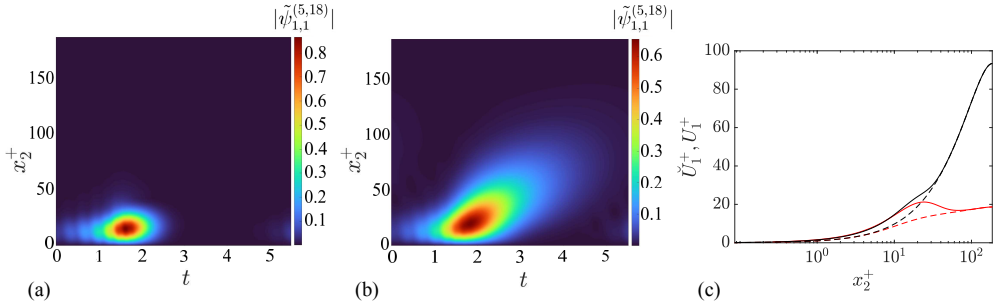

FIGURE 6. Magnitude of the streamwise component of the primary perturbation (equivalently, optimal linear streak) $|\tilde{\sigma}^{(5,18)}\tilde{\boldsymbol{\psi}}_{1,1}^{(5,18)}|$ computed for the larger channel using (a) the laminar mean profile and (b) the turbulent mean profile at $Re_\tau = 186$. (c) The streamwise base flow $\breve{U}_1$ at peak t and x_3 for the laminar (solid black) and turbulent (solid red) cases, with the original laminar (dashed black) and turbulent (dashed red) shown for comparison.

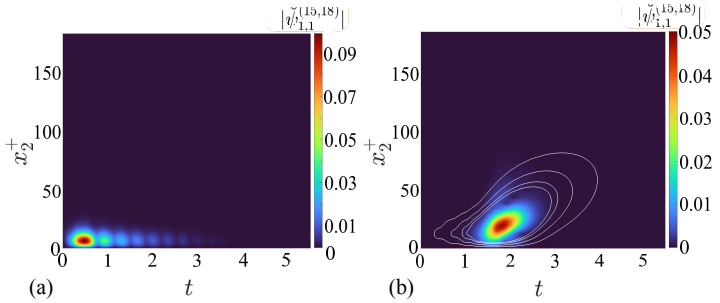

FIGURE 7. Magnitude of the streamwise component of a secondary perturbation $|\breve{\sigma}^{(15,18)}\breve{\boldsymbol{\psi}}_{1,1}^{(15,18)}|$ computed using the turbulent mean profile of the larger channel at $Re_\tau = 186$, for (a) $N_s = 1$ (b) $N_s = 13$. White lines in (b) indicate the primary streak contours (25%, 50%, 75%, and 90% of the maximum).

contains the buffer layer of the turbulent mean profile. The optimal transient primary perturbation (streak) is shown in Figure 6.

As in the previous section, we first compute α–spectra for $N_s = 1$, windowing the forcing mode to a scaling function with shift $m = 0$, which corresponds to actuating the lower half of the resolved temporal frequencies. We also compute spectra that take into account the interactions with the primary and without restricting the forcing in time or frequency. For a central mode (k_1°, k_3°), the set of coupled modes is $\mathcal{S} = \{(k_1^\circ + 2is_1^\circ, k_3^\circ + 2js_3^\circ)\}_{i,\,j=-1}^{1} \cup \{(k_1^\circ + is_1^\circ, k_3^\circ + js_3^\circ)\}_{i,\,j=-1,1}$, where $(s_1^\circ, s_3^\circ) = (5, 18)$. Each additional mode is coupled to one or two others through a dyadic interaction that involves $(\pm s_1^\circ, \pm s_3^\circ)$ and $N_s = 13$. The target modes are chosen from $k_1^\circ \in [0, 52]$, $k_3^\circ \in [9, 76]$. An example mode is shown in Figure 7 to illustrate the effect of the primary streak interaction on the mode shape. To compute α, we use $\tau = 1.6$, which corresponds to the kinetic energy peak of the primary perturbation $\boldsymbol{\psi}_1^{(5,18)}$ for both the laminar and turbulent means.

The α–spectra computed from laminar and turbulent means for $N_s = 1$ [Figure 8(a, b)] exhibit peaks at $k_1^\circ = 15$ at $x_2^+ \approx 12$. The resolvent dissipation α^2 for other scales seems to be negligible. A weaker secondary peak appears for $k_1^\circ = 10$. In the E_ω–spectrum

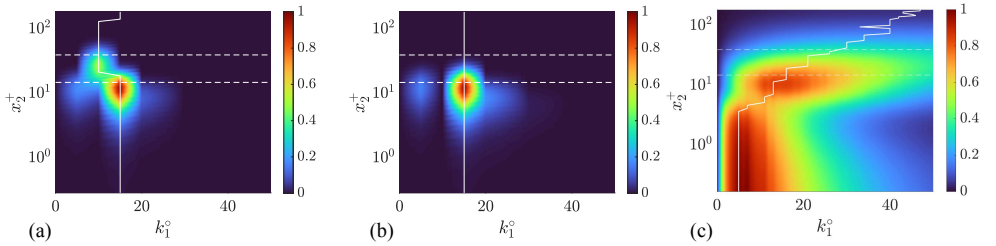

FIGURE 8. Larger channel dissipation α^2 with $N_s = 1$, normalized by the maximum over x_2 and k_1 and using (a) the laminar mean and (b) the turbulent mean; (c) represents the surrogate dissipation from the DNS of the minimal channel. The values are normalized by the maximum value across all k_1° and x_2; the solid white line represents the x_2–local maximum across k_1° values, and the dashed horizontal lines mark the limits of the buffer layer $x_2^+ = 15$ and $x_2^+ = 40$.

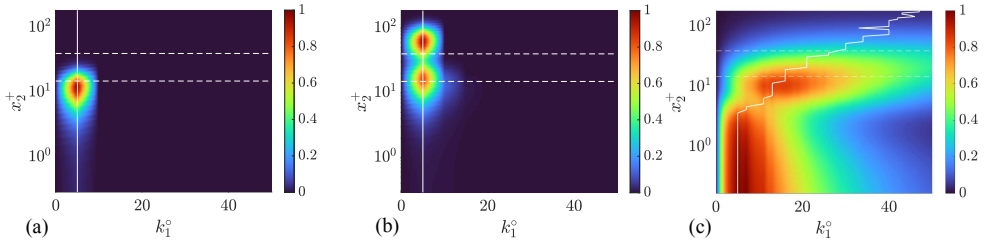

FIGURE 9. Larger channel dissipation α^2 with $N_s = 13$, normalized by the maximum over x_2 and k_1 and using (a) the laminar mean and (b) the turbulent mean; (c) represents the surrogate dissipation from the DNS of the minimal channel. The values are normalized by the maximum value across all k_1° and x_2; the solid white line represents the x_2–local maximum across k_1° values, and the dashed horizontal lines mark the limits of the buffer layer $x_2^+ = 15$ and $x_2^+ = 40$.

[Figure 8(c)], most of the dissipation occurs for $x_2^+ < 40$ and for wave numbers $k_1^\circ < 50$. Wave number $k_1^\circ = 5$, corresponding to the streamwise wave number of near-wall streaks, dominates in the region $x_2^+ \in [0, 5]$; in a region centered around $x_2^+ \approx 12$ near the bottom of the buffer layer, smaller structures corresponding to $k_1^\circ \in [10, 30]$ are the most dissipative. The α–spectra correctly identify $k_1^\circ \approx 15$ structures as significantly dissipative at $x_2^+ \approx 12$, but fail to capture the importance of $k_1^\circ = 5$ near the wall. Moreover, the peak in the α–spectra is narrower: they overrepresent the importance of $k_1^\circ \approx 15$ structures with respect to similar scales.

In Figure 9, we plot the α–spectra that take into account the coupling with the primary streak. In these spectra, the streak scale $k_1^\circ = 5$ is the most significant across the entire channel when both the laminar and turbulent means are used. Moreover, the peak occurs in the former at $x_2^+ \approx 12$ and in the latter at $x_2^+ \approx 66$, though the turbulent spectrum also exhibits a secondary peak at $x_2^+ \approx 15$.

We note that when we consider multiscale interactions enabled by the primary mode, the α–spectrum skews toward scales more similar to the primary. In the resolvent framework formulated in Section 2, velocity fluctuations have two sources of energy: the base flow (which may include the primary perturbation) or the forcing term, which represents energy from external scales. Scales of motion that, in DNS, are energized by interactions between the streak scale and the mean ($k_1^\circ = 5$), or self-interactions within the streak

($k_1^\circ = 10$), are thus expected to be better modeled by these resolvent modes than scales that are much smaller or much larger. To confirm this, the nonlinear energy transfer spectrum (Symon *et al.* 2021; Ballouz *et al.* 2025; Ding *et al.* 2025) must show that the primary $(k_1^\circ, k_3^\circ) = (5, 18)$ sheds its energy to other $k_1^\circ = 5$ scales preferentially. This would also explain the underestimated contribution of smaller scales to the α–spectrum. For the purpose of tuning RNL models, a combined approach using both $N_s = 1$ and $N_s > 1$ is best. This ensures that we capture the contributions of both the scales that benefit preferentially from interactions with the near-wall streaks and the smaller scales that seem to feed off other intermediate scales in the turbulent cascade.

Another observation is that, as in the minimal channel case, the normalized α–spectrum differs little whether a laminar or a turbulent mean profile is used. The base flow moderately affects the shape and amplification of primary and secondary modes [Figure 6(a,b)], but the composite base flow profile for both the laminar and turbulent cases are similar for $x_2^+ < 12$, which may explain why both profiles have similar linear amplification properties. In light of these similarities, the use of the laminar system in the construction of α–spectra is justified. Past and recent work in optimal linear growth theory, which tends to study fluctuations about the laminar mean, has also been used to glean insights into the mechanics of turbulent flows (Farrell & Ioannou 1998; Markeviciute & Kerswell 2024).

4. Conclusions and next steps

The main contribution of this work is to introduce a resolvent analysis-based methodology for the purpose of studying secondary coherent structures that feed off the primary coherent structure, that is, near-wall streaks in channel flow. Resolvent analysis was fruitful for understanding the linearly driven growth of these streamwise streaks from streamwise rolls; we adapt it to identify the scales that lead to the breakdown of these streaks. More generally, the newly developed framework can be used to study secondary coherent structures—secondary in the sense that they tend to be less energetic—that curtail the growth of primary ones.

We apply the methodology to construct a cheaper alternative to the surrogate dissipation spectrum that does not require a prior DNS. These spectra can then be used to tune RNL models. The results presented are promising: for both the minimal channel and, to a lesser degree, the larger channel, the resolvent-based α-spectra correctly identify the key length scales that account for hot spots in the DNS-based surrogate dissipation spectrum. However, the α–spectrum for the larger channel highlights a much restricted subset of these relevant length scales and underestimates the role of high wave numbers. To remedy this, since scales close to the primary tend to be preferred in the α–spectrum of the larger channel, we propose using a smaller primary mode, for example, $(\lambda_1^+, \lambda_3^+) = (500, 50)$, which may increase the contribution of smaller dissipative scales. Another option is to redefine the semi-norm that the SVD at the core of resolvent analysis maximizes. Typically, resolvent analysis seeks to maximize the kinetic energy of the response mode. One could instead maximize a dissipation semi-norm, that is,

$$\int_\ell \int_m \int_0^2 |k_1^2 \tilde{\boldsymbol{\psi}}_{\mathbf{1,1}}|^2 + \left| \frac{d^2}{dx_2^2} \tilde{\boldsymbol{\psi}}_{\mathbf{1,2}} \right|^2 + |k_3^2 \tilde{\boldsymbol{\psi}}_{\mathbf{1,3}}|^2 dx_2 dm d\ell, \tag{4.1}$$

in an attempt to highlight the smaller scales.

The usefulness of this methodology lies in its ability to replace surrogate dissipation

spectra. The cost of converged surrogate dissipation spectra increases significantly with Reynolds number, and it would therefore be valuable to test the applicability of α-spectra to flows at moderate and high Re_τ. This constitutes the next step of this project with the potential for the highest impact.

Acknowledgements: The support of ONR to CTR under grant N000142312833 is gratefully acknowledged.

REFERENCES

Adrian, R. J. 2007 Hairpin vortex organization in wall turbulence. *Phys. Fluids* **19**, 041301.

Bae, H. J., Lozano-Durán, A., Bose, S. T. & Moin, P. 2019 Dynamic slip wall model for large-eddy simulation. *J. Fluid Mech.* **859**, 400–432.

Bae, H. J., Lozano-Durán, A., Bose, S. T. & Moin, P. 2018 Turbulence intensities in large-eddy simulation of wall-bounded flows. *Phys. Rev. Fluids* **3**, 014610.

Bae, H. J., Lozano-Durán, A. & McKeon, B. J. 2021 Nonlinear mechanism of the self-sustaining process in the buffer and logarithmic layer of wall-bounded flows. *J. Fluid Mech.* **914**, A3.

Bakewell Jr., H. P. & Lumley, J. L. 1967 Viscous sublayer and adjacent wall region in turbulent pipe flow. *Phys. Fluids* **10**, 1880–1889.

Ballouz, E., Dawson, S. T. M. & Bae, H. J. 2025 Transient growth and nonlinear breakdown of wavelet-based resolvent modes in turbulent channel flow. *J. Fluid Mech.* **1016**, A19.

Ballouz, E., Lopez-Doriga, B., Dawson, S. T. M. & Bae, H. J. 2024 Wavelet-based resolvent analysis of non-stationary flows. *J. Fluid Mech.* **999**, A53.

Blackwelder, R. F. & Eckelmann, H. 1979 Streamwise vortices associated with the bursting phenomenon. *J. Fluid Mech.* **94**, 577–594.

Bretheim, J. U., Meneveau, C. & Gayme, D. 2015 Standard logarithmic mean velocity distribution in a band-limited restricted nonlinear model of turbulent flow in a half-channel. *Phys. Fluids* **27**, 011702.

Daubechies, I. 1992 *Ten lectures on wavelets*. SIAM.

Ding, J., Chung, D. & Illingworth, S. J. 2025 Mode-to-mode nonlinear energy transfer in turbulent channel flows. *J. Fluid Mech.* **1002**, A42.

Farrell, B. F. & Ioannou, P. J. 1998 Perturbation structure and spectra in turbulent channel flow. *Theor. Comput. Fluid Dyn.* **11** (3), 237–250.

Gayme, D. F. & Minnick, B. A. 2019 Coherent structure-based approach to modeling wall turbulence. *Phys. Rev. Fluids* **4**, 110505.

Gorski, J. J., Wallace, J. M. & Bernard, P. S. 1994 The enstrophy equation budget of bounded turbulent shear flows. *Phys. Fluids* **6**, 868100.

Hamilton, J. M., Kim, J. & Waleffe, F. 1995 Regeneration mechanisms of near-wall turbulence structures. *J. Fluid Mech.* **287**, 317–348.

Huang, Y., Toedtli, S. S., Chini, G. P. & McKeon, B. J. 2025 Spatio-temporal characterization of nonlinear forcing and response in turbulent channel flow. arXiv:2503.06915 [physics.flu-dyn] .

Hutchins, N. & Marusic, I. 2007 Large-scale influences in near-wall turbulence. *Philos. Trans. R. Soc. A* **365**, 647–664.

Jiménez, J. 2012 Cascades in wall-bounded turbulence. *Annu. Rev. Fluid Mech.* **44**, 27–45.

Jiménez, J. 2018 Coherent structures in wall-bounded turbulence. *J. Fluid Mech.* **842**, P1.

Jiménez, J. & Moin, P. 1991 The minimal flow unit in near-wall turbulence. *J. Fluid Mech.* **225**, 213–240.

Johansson, A. V., Her, J.-Y. & Haritonidis, J. H. 1987 On the generation of high-amplitude wall-pressure peaks in turbulent boundary layers and spots. *J. Fluid Mech.* **175**, 119–142.

Kim, H. T., Kline, S. J. & Reynolds, W. C. 1971 The production of turbulence near a smooth wall in a turbulent boundary layer. *J. Fluid Mech.* **50**, 133–160.

Kim, J. & Moin, P. 1985 Application of a fractional-step method to incompressible Navier-Stokes equations. *J. Comput. Phys.* **59**, 308–323.

Klebanoff, P. S., Tidstrom, K. D. & Sargent, L. M. 1962 The three-dimensional nature of boundary-layer instability. *J. Fluid Mech.* **12**, 1–34.

Kline, S. J., Reynolds, W. C., Schraub, F. A. & Runstadler, P. W. 1967 The structure of turbulent boundary layers. *J. Fluid Mech.* **30**, 741–773.

Landahl, M. T. 1980 A note on an algebraic instability of inviscid parallel shear flows. *J. Fluid Mech.* **98**, 243–251.

Lozano-Durán, A. & Bae, H. J. 2016 Turbulent channel with slip boundaries as a benchmark for subgrid-scale models in LES. *Annual Research Briefs*, Center for Turbulence Research, Stanford University, pp. 97–103.

Lozano-Durán, A., Constantinou, N. C., Nikolaidis, M.-A. & Karp, M. 2021 Cause-and-effect of linear mechanisms sustaining wall turbulence. *J. Fluid Mech.* **914**, A8.

Mallat, S. 1999 *A wavelet tour of signal processing*. Elsevier.

Markeviciute, V. K. & Kerswell, R. R. 2024 Threshold transient growth as a criterion for turbulent mean profiles. *J. Fluid Mech.* **996**, A32.

Marusic, I. 2001 On the role of large-scale structures in wall turbulence. *Phys. Fluids* **13**, 735–743.

McKeon, B. J. 2017 The engine behind (wall) turbulence: perspectives on scale interactions. *J. Fluid Mech.* **817**, P1.

McKeon, B. J. & Sharma, A. S. 2010 A critical-layer framework for turbulent pipe flow. *J. Fluid Mech.* **658**, 336–382.

Minnick, B. A. & Gayme, D. 2019 Characterizing energy transfer in restricted nonlinear wall-bounded turbulence. In *TSFP11*, pp. 145–150. Danbury, CT: Begell.

Minnick, B. A., Viggiano, B. & Gayme, D. F. 2023 Augmented restricted nonlinear (ARNL) model for high Reynolds number wall-turbulence. In *iTi*, pp. 65–75. Cham, Switz.: Springer.

Moarref, R., Sharma, A. S., Tropp, J. A. & McKeon, B. J. 2013 Model-based scaling of the streamwise energy density in high-Reynolds-number turbulent channels. *J. Fluid Mech.* **734**, 275–316.

Monty, J. P., Stewart, J. A., Williams, R. C. & Chong, M. S. 2007 Large-scale features in turbulent pipe and channel flows. *J. Fluid Mech.* **589**, 147–156.

Najmi, A.-H. 2012 *Wavelets: A concise guide*. JHU Press.

Orlandi, P. 2000 *Fluid Flow Phenomena: A Numerical Toolkit*. Springer Science & Business Media, Vol. 55. Kluwer Acadmic Publishers.

Padovan, A., Otto, S. E. & Rowley, C. W. 2020 Analysis of amplification mechanisms and cross-frequency interactions in nonlinear flows via the harmonic resolvent. *J. Fluid Mech.* **900**, A14.

Panton, R. L. 2001 Overview of the self-sustaining mechanisms of wall turbulence. *Prog. Aerosp. Sci.* **37**, 341–383.

Robinson, S. K. 1991 Coherent motions in the turbulent boundary layer. *Annu. Rev. Fluid Mech.* **23**, 601–639.

Schmid, P. J., Henningson, D. S. & Jankowski, D. F. 2002 *Stability and Transition in Shear Flows.*. Appied Mathematical Sciences, Vol. 142. Springer-Verlag.

Smith, C. R. & Metzler, S. P. 1983 The characteristics of low-speed streaks in the near-wall region of a turbulent boundary layer. *J. Fluid Mech.* **129**, 27–54.

Smits, A. J., McKeon, B. J. & Marusic, I. 2011 High–Reynolds number wall turbulence. *Annu. Rev. Fluid Mech.* **43**, 353–375.

Symon, S., Illingworth, S. J. & Marusic, I. 2021 Energy transfer in turbulent channel flows and implications for resolvent modelling. *J. Fluid Mech.* **911**, A3.

Waleffe, F. 1997 On a self-sustaining process in shear flows. *Phys. Fluids* **9**, 883–900.

Wray, A. A. 1990 Minimal storage time advancement schemes for spectral methods. *Tech. Rep. No. 202,* NASA Ames Research Center .